Applicability of different geometry approaches to simulations of turbulence in highly sheared magnetic fields

D. Told and F. Jenko
Max-Planck-Institut für Plasmaphysik, Boltzmannstr. 2, D-85748 Garching, Germany

For more than a decade, Eulerian simulations of plasma turbulence have been using coordinate systems aligned to the background magnetic field in order to exploit the elongated structure of the turbulent eddies. Here, two possible setups of such field-aligned coordinate systems are studied with regard to their behavior under more extreme conditions such as tokamak edge or stellarator geometries, where large global and/or local shear are encountered. Turbulence codes employing a Fourier expansion are shown to yield correct solutions also for large shear values, given that the radial resolution chosen is large enough. Codes which compute the radial direction in real space, on the other hand, can benefit from the implementation of the shifted metric approach, which may save resolution in the case of large shear.

I. INTRODUCTION

In the course of the past two decades, turbulence simulations have emerged as a useful tool to gain insight into the mechanisms that govern heat, momentum, and particle transport processes in magnetized plasmas as found in fusion experiments like tokamaks and stellarators.

Experimentally, it has been known for years that plasma confinement in such devices can be much enhanced in a diverted geometry, facilitating the transition to the H-mode regime [1]. In divertor geometry, the last closed flux surface (separatrix) is not circular anymore as in earlier experiments, and experience shows that confinement can be further enhanced by distorting the plasma shape in an elliptical and/or triangular fashion.

Traditionally, analytical and numerical studies of plasma turbulence were based mostly on the $\hat{s} - \alpha$ model, which resembles a large-aspect ratio tokamak with circular cross-section [2]. While this model has proven very useful for basic turbulence studies, it lacks the accuracy that is necessary for a quantitative comparison of simulation and experiment. This is particularly true for simulations of the tokamak edge, where flux surfaces deviate substantially from the circular shape and the metric coefficients show a strong parallel dependence, which is not accurately taken into account in analytical models. In addition, close to the separatrix, the safety factor, and thus also magnetic shear, diverge to infinity, so that large global shear values must be taken into account correctly by turbulence codes.

Stellarator devices, on the other hand, are not axisymmetric like tokamaks, and therefore geometric quantities depend strongly on the parallel coordinate (see, e.g. Ref. [3]) even in the core. In contrast to the large values of global (i.e. flux surface averaged) magnetic shear that are encountered in the tokamak edge, stellarators are generally designed such that their rotational transform (the inverse safety factor) covers only a small range of values. Global shear values therefore tend to be low. Due to the strong parallel variation of the geometry, on the other hand, considerable local shearing may occur. In this work, we will therefore examine two established types of field-aligned coordinate systems, their applicability to different types of turbulence codes and their behavior in complex geometries.

The paper is structured as follows: In Section II, we describe some properties of field-aligned coordinate systems, along with a discussion of the differences between standard and shifted metric. In Section III, we describe the numerical tool we employ for this study, and show results of linear and nonlinear simulations with both types of geometry. Section IV provides the theoretical understanding of the numerically obtained results, and in Section V we draw some conclusions.

II. PROPERTIES OF FIELD-ALIGNED COORDINATE SYSTEMS

As has already been mentioned, it is common for plasma turbulence codes to employ a spatial coordinate system which is aligned to the magnetic field. Such a treatment takes advantage of the fact that in strongly magnetized plasmas all particles experience the Lorentz force. While this does not affect their parallel motion much, perpendicular motion can only occur due to drift effects, which can be caused, e.g., by magnetic field inhomogeneities and electric fields. Since typical drift velocities are much slower than thermal velocities, the turbulent eddies that are found under such conditions show an elongated structure, with parallel correlation lengths that can exceed their perpendicular counterparts by orders of magnitude. In field-aligned coordinates (and only there), it is therefore possible to use only few grid nodes to cover many meters along the field line, while at the same time resolving sub-millimeter scales perpendicular to the magnetic field.

In the literature, there exist numerous derivations of field-aligned coordinates (see, e.g. Refs. [4–7]), which we will not repeat here. Instead we will give a description of some properties of these coordinate systems. In addition to the standard field-aligning approach, one of the aforementioned works [7] also defined a 'shifted-metric' approach, which differs from the former one in several aspects that we wish to illuminate.

A. Magnetic shear in straight and shifted metric

In the usual transformation from cylindric to field-aligned coordinates, one defines a set of three coordinates x, y, z, which represent the radial, binormal and parallel directions,

respectively. For convenience, one often chooses the reference position to be where the contravariant $\boldsymbol{e}^x = \nabla x$ vector is parallel to the cylindrical $\boldsymbol{e}^r = \nabla r$, i.e. where the flux surface is perpendicular to the (cylindrical) radial direction. For up-down symmetric geometries, this is the outboard midplane. The $\boldsymbol{e}^y$ vector, on the other hand, lies in the flux surface, perpendicular to the field line direction. However, the x and y coordinate vectors are only orthogonal at the aforementioned reference position, which can be seen as follows: Since the safety factor is not constant across the minor plasma radius, the pitch of the magnetic field changes between different radii. At the reference position, where y (the field line label) can be defined to be zero for all radial positions, a small step in direction of $\boldsymbol{e}^x$ changes only the x coordinate. At a different parallel position, however, a small step in x direction will in general be accompanied by a change of the y coordinate, since the field lines with $y = 0$ that we started with are now at different poloidal angles due to the differing safety factor. This means that $\boldsymbol{e}^y = \nabla y$ now has a radial component, so that $g^{xy} = \nabla x \cdot \nabla y \neq 0$ when departing from the outboard midplane. Therefore, the perpendicular grid is only orthogonal at the reference position where y is defined to be zero for all radial positions. As one follows the field line, the angle between the $\boldsymbol{e}^x$ and $\boldsymbol{e}^y$ vectors increases according to magnetic shear (or local shear, if its parallel dependence is taken into account, see, e.g., Ref. [8]).

The shifted-metric approach which has been first described in Ref. [7], avoids these complications by introducing a different coordinate y_k for every position z_k along the field line. This y_k is defined such that $g^{xy_k} = 0$ everywhere, which requires the following definition:

$$y_k = y - \frac{g^{xy}}{g^{xx}}\Big|_k x, \tag{1}$$

where the metric coefficient g^{xy} is to be calculated with the unshifted y coordinate, at position z_k. We note that the same transformation is also applied in simulations employing the standard Clebsch approach, but only at the parallel ends of the simulation domain, and with the integrated coefficient $\int (g^{xy}/g^{xx}) dz = 2\pi\hat{s}$. In the shifted metric case, on the other hand, the shift of the y coordinate is split into as many pieces as there are parallel points in the simulation.

B. Adaptation of parallel derivatives for shifted metric

Since each parallel position now has a different y coordinate, the calculation of parallel derivatives must be adapted to account for the shifts, as has also been shown in Ref. [7]. As various gyrokinetic codes like GS2 [9, 10], GKW [11] and GENE [12–15] compute the perpendicular dynamics in Fourier space, we will give a short repetition of the calculation for such cases. If the parallel derivatives are computed via fourth-order centered finite differences, then the function values from two neighboring points in each direction enter the computation. In the shifted metric case, the coordinate system changes from point to point, so that in order to calculate the derivative of $f(z)$ at parallel position k, one has to perform the following operation on data from position $k + i$: First execute an inverse shifted metric transformation $y_{k+i} \rightarrow y$ (changing from the coordinate system at point $k + i$ to the field-aligned reference system), then transform $y \rightarrow y_k$ (back to the shifted coordinate at position k). The complete transformation is therefore:

$$y_k = y_{k+i} + \left(\frac{g^{xy}}{g^{xx}}\Big|_{k+i} - \frac{g^{xy}}{g^{xx}}\Big|_k \right) \cdot x \equiv y_{k+i} + \chi_{ki} \cdot x \tag{2}$$

Thus, when using a value of f from parallel point $k + i$, we have to apply the following shift when calculating the derivative in terms of the coordinates at point k:

$$f(x, y_{k+i}, z_{k+i})\big|_{y_{k+i}} \rightarrow f(x, y_k - \chi_{ki} \cdot x, z_{k+i})\big|_{y_k} \tag{3}$$

Here, the label $\big|_{y_{k+i}}$ is used to signify that the value has been evaluated in the coordinate system y_{k+i}. Due to the discretization, in a real-space treatment an interpolation will in general be required (especially in complicated geometries, where χ_{ki} can take arbitrary values) to calculate the function values at the actual spatial grid points. Performing a Fourier transform only in the y direction on the right hand side of the above condition yields:

$$\begin{aligned} &f(x, k_y, z_{k+i})\big|_{y_k} \\ &\quad = \int_{-\chi_{ki}\cdot x}^{L_y - \chi_{ki}\cdot x} f(x, y_k - \chi_{ki} \cdot x, z_{k+i}) \mathrm{e}^{-ik_y y_k} dy_k \end{aligned} \tag{4}$$

Now we shift the y_k coordinate to y_{k+i}:

$$\begin{aligned} &\int_0^{L_y} f(x, y_{k+i}, z_{k+i}) \mathrm{e}^{-ik_y(y_{k+i} + \chi_{ki}\cdot x)} dy_{k+i} \\ &\qquad = f(x, k_y, z_{k+i})\big|_{y_{k+i}} \mathrm{e}^{-ik_y \chi_{ki} \cdot x} \end{aligned} \tag{5}$$

Therefore, when using function values from neighboring parallel positions, these values have to be multiplied by a phase factor:

$$f(x, k_y, z_{k+i})\big|_{y_k} = f(x, k_y, z_{k+i})\big|_{y_{k+i}} \mathrm{e}^{-ik_y \chi_{ki} \cdot x} \tag{6}$$

If the x direction is also treated in Fourier space, the transformation reads:

$$f(k_x, k_y, z_{k+i})\big|_{y_k} = f(k_x + k_y \chi_{ki}, k_y, z_{k+i})\big|_{y_{k+i}} \tag{7}$$

C. Radial boundary conditions

According to Eq. (7), the shift in y is associated (in Fourier space) to a mode shift in k_x (see also Ref. [6]). Applying the shifted metric to a code which computes both perpendicular directions in Fourier space is therefore only possible if all k_x

modes that can occur due to the shifts are present in the system. While in the standard field-aligned approach, the only k_x shifts occur at the parallel ends of the box, the shifts are much smaller in the shifted metric case. To ensure the same radial resolution, a much larger number of k_x modes would be necessary to allow for the shifts. Furthermore, the shifts can be arbitrary in general geometry, so that no straightforward implementation for local Fourier codes is possible.

If, on the other hand, only the y direction is treated in Fourier space, the shifts in that direction become a multiplication with a phase factor (see Eq. 6), so that in principle arbitrary shifts become possible. If one wants to emulate flux-tube simulations with such an implementation, however, one has to take into account that the phase shifts can violate the radial periodic boundary condition that is used in the flux-tube model [6, 7]. Since the phase factor depends on k_y, periodicity can only be fulfilled if the radial box extension L_x is chosen such that the phase factor becomes a multiple of $\exp(i\pi)$ at the radial boundary for each k_y mode. This can, depending on the shear value, force one to use very large radial box sizes (corresponding to the small k_x shifts from above) in order to fulfill the periodic boundary condition for every k_y mode—in that case one would face the same problem as in a fully spectral code. Note, however, that nonlocal simulations can only be performed with non-periodic boundaries, e.g. of Dirichlet or von-Neumann type, for which the shifted metric does not cause any problem.

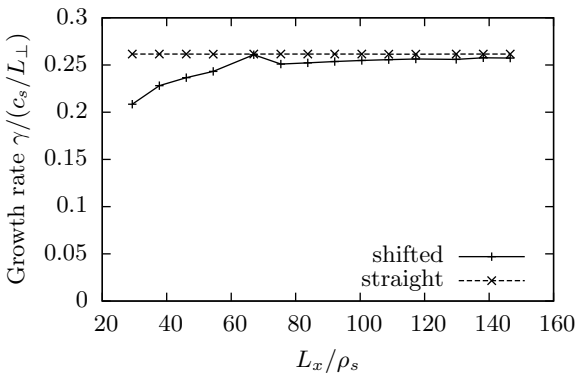

FIG. 1: Convergence of linear growth rates with increasing radial box size, using periodic boundary conditions.

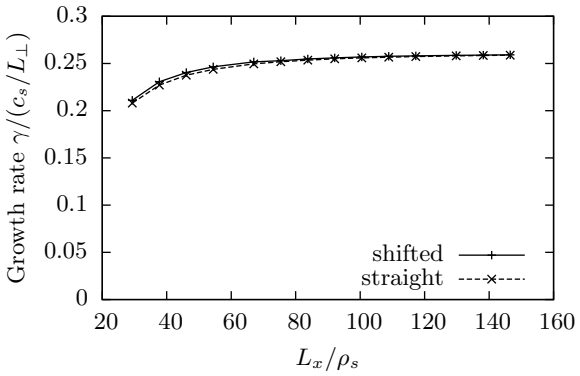

FIG. 2: Convergence of linear growth rates with increasing radial box size, using Dirichlet boundary conditions.

III. NUMERICAL TESTS OF STANDARD AND SHIFTED METRIC

A. The GENE code

For the simulations shown in this study, we employ the gyrokinetic turbulence code GENE [12–15]. Since we intend to focus on very basic features of the numerical treatment, the physical complexity is kept low by using only one species (ions) and considering the electrons as adiabatic. Effects like magnetic fluctuations, collisions and nonlocal effects are neglected. For more physically comprehensive simulations of various plasma conditions, see e.g. Refs. [16–19].

The GENE code allows to choose between two different modes of operation; the first one employs a Fourier space flux-tube treatment with periodic boundary conditions in both perpendicular directions, while the second setting treats only the y direction in Fourier space. The radial dynamics, instead, are treated in real space with nonperiodic boundary conditions in order to allow for radial profile variations. As we have shown in section II B, an easy implementation of the shifted metric is only possible for the latter operation mode. Therefore, all simulations with shifted metric have been carried out with the nonlocal version, emulating however the local simulations without profile variation.

B. Effect of radial boundary conditions

To compare the convergence of both shifted and straight (standard) metric with Dirichlet and periodic boundary conditions, we performed some linear simulations in a Cyclone Base Case [20] parameters set, choosing $k_y \varrho_s = 0.3$ and increasing the radial box size L_x and the number of radial points simultaneously in order to keep the resolution constant. Fig. 1 shows the convergence behavior for periodic boundary conditions. With this approximation, the flux tube simulation always gives the same result, while the shifted metric simulation converges to within 10% of the flux tube result for $L_x \gtrsim 50\varrho_s$. At a value of $L_x \approx 67\varrho_s$, the shifted metric result is identical to the flux tube one, since with this L_x the periodic boundary condition is exactly fulfilled. The same would also be visible at $L_x \approx 2 \cdot 67\varrho_s = 134\varrho_s$, but that point is not included in the scan. For Dirichlet boundaries, on the other hand (see Fig. 2), the speed of convergence is almost identical for both shifted and straight metric, reaching an accuracy of 10% as soon as $L_x \gtrsim 50\varrho_s$. Thus, for nonlocal simulations, the impact of the radial boundary condition on the simulation is the same for both the straight and shifted metric approach.

C. Nonlinear simulations with straight and shifted metric

In Ref. [7], it was found that turbulence simulations employing standard field-aligned coordinates become inaccurate when studying conditions with large (global) magnetic shear: Although a sheared slab geometry was used, in which, due to the absence of curvature effects, the heat flux at all parallel points should be equal, it was found that parallel transport profiles yielded a 'ballooned' structure, i.e. the transport value decreased from the center towards the ends of the flux tube. As a remedy, the shifted-metric approach was put forward, which was able to eliminate the artificial structure.

As we have seen above, however, for a flux tube code with periodic boundaries (like the local GENE version), the shifted metric approach can not be easily implemented. Therefore, we will now study if the standard approach leads to similar problems in a Fourier treatment, and if there is a possibility to overcome them. In Ref. [7], a four-field model was employed that described the nonlinear electron dynamics while assuming cold ions. The physical model thus differs clearly from the kinetic ion/adiabatic electron model that we employ in our study; as we will see, however, both models deliver very comparable results with respect to the geometric properties discussed here. For the first simulation, we choose a grid of $60\varrho_s \times 20\pi\varrho_s$ in the perpendicular plane, with a resolution of $32 \times 32 \times 16 \times 32 \times 8$ grid points in the x, y, z, $v_\parallel$ and μ directions, respectively, keeping the same resolution as in the original simulations (but using a smaller box in y direction). The gradients are selected such that ion temperature gradient modes are unstable ($L_\parallel/L_T = 10$, $L_\parallel/L_n = 2.2$), and global shear is set to unity to match the metric from Ref. [7]. In Fig. 3, the parallel heat flux profile obtained from this simulation is depicted. Near the parallel boundaries, zig-zag structures appear which indicate insufficient resolution. This result differs from the one in Ref. [7] in that it can be clearly recognized as a numerical deficiency, while in the original work, there was a smooth reduction in transport towards the parallel boundaries, which could not be distinguished from the natural ballooning effect one would expect in a toroidal geometry.

As we will illuminate in more detail in the following sections, increasing the magnetic shear value will require an according increase in the radial resolution. Indeed, as it turns out, the zig-zag structures found in the parallel heat flux profiles vanish only when using four times the resolution compared to the initial setup, yielding a completely flat profile (see Fig. 4) then. For a shear value of $\hat{s} = 2$, this is achieved at a resolution of $n_x = 192$ (Fig. 5).

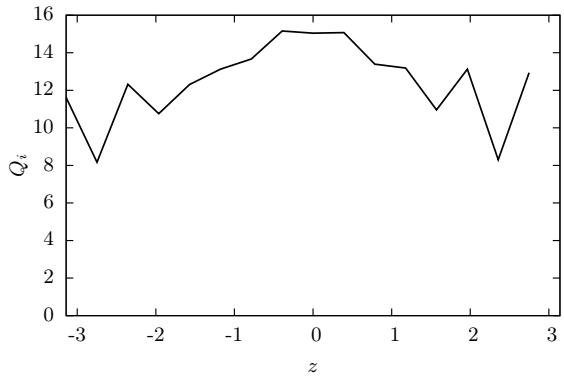

FIG. 3: Parallel heat flux profile for a nonlinear slab simulation with global shear $\hat{s} = 1$ and 32 radial grid nodes.

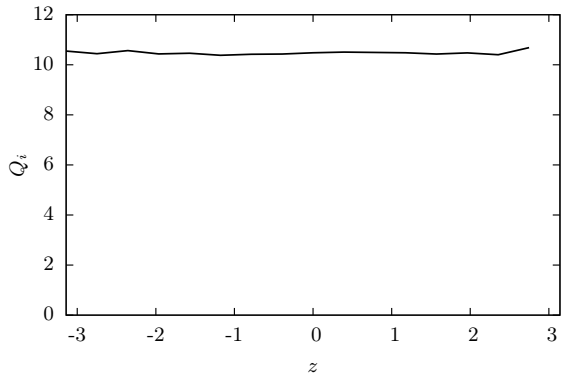

FIG. 4: Parallel heat flux profile with global shear $\hat{s} = 1$ and 128 radial grid nodes.

D. Influence of numerical schemes

To illuminate the origin of the numerical problems that arise at high magnetic shear, we will first compare the numerical treatments of the perpendicular direction that were used in the original and our simulations: In the original work, a second-order upwind scheme was employed [21], whereas the local GENE simulation uses a Fourier treatment, which yields exact derivatives (limited only by machine accuracy). The upwind scheme is intrinsically dissipative, which on the one hand serves to eliminate detrimental aliasing effects by damping small-scale structures. On the other hand, we will see that in combination with the field-aligned coordinates, the dissipation of the scheme facilitates the appearance of the observed spurious ballooning, while at the same time masking its numerical origin.

The necessity of employing some kind of dealiasing scheme in gyrokinetic turbulence codes stems from the fact that the gyrokinetic Vlasov equation as used in the GENE code [14] contains a quadratic nonlinearity, given by

$$\mathcal{N}(\boldsymbol{k},\boldsymbol{k}') = \frac{\partial\chi}{\partial y}\frac{\partial g_j}{\partial x} - \frac{\partial\chi}{\partial x}\frac{\partial g_j}{\partial y} = \sum_{\boldsymbol{k}'}(k'_x k_y - k_x k'_y)\chi(k')g_j(k-k'), \quad (8)$$

where $\chi = \Phi - v_{Tj}v_\parallel A_{\parallel j}$ is the modified potential and $g_j = f_j + 2v_\parallel A_{\parallel j}F_M q_j/m_j v_{Tj}$ is the modified distribution function. This nonlinear term couples different wavenumbers and thus causes an excitation of waves with larger wavenumbers than are actually contained in the system. These are then erroneously interpreted as lower wavenumbers, resulting in a transfer of energy to larger scales, which often leads to a

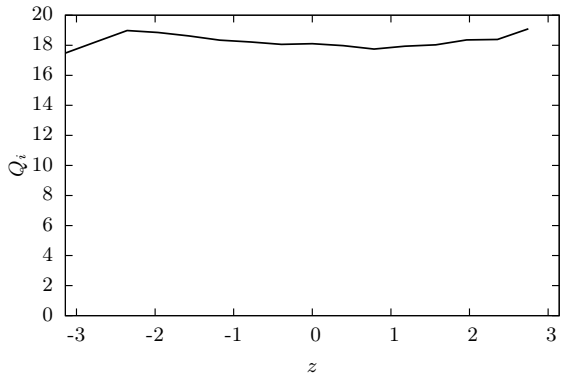

FIG. 5: Parallel heat flux profile with global shear $\hat{s} = 2$ and $n_x = 192$. Note that the temperature scale length has been increased to $L_\parallel/L_T = 15$ to compensate for the larger shear value.

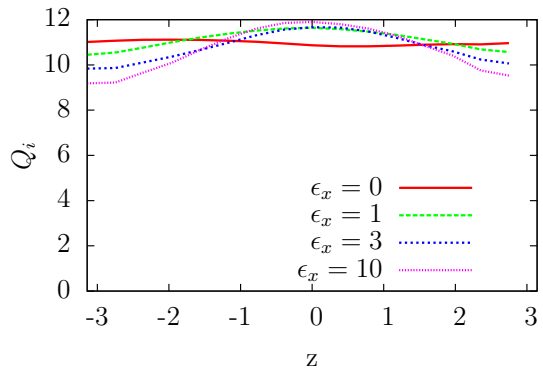

FIG. 6: (Color online) With increasing radial hyperdiffusion coefficient ϵ_x, the parallel heat flux profile exhibits an increasing amount of unphysical ballooning.

'blow-up' of the simulation. To avoid this kind of numerical instability, often a numerical diffusion term is introduced to damp the high-k contributions and thus eliminate this aliasing effect. In Ref. [7], this numerical diffusion is included implicitly in the upwind scheme employed there.

In GENE , on the other hand, the Fourier space treatment allows to use the three-halves rule due to Orszag [22] to prevent aliasing: For the computation of the nonlinearity (which is done in real space to avoid computing the convolution in the right hand side of Eq. 8), the wavenumber grid is zero-padded in k_x and k_y directions with $n_x/2$ or $n_y/2$ modes, respectively. After calculating the nonlinearity, these modes are discarded again and the computation continues on the smaller grid. Therefore, nonlinear simulations can usually be performed without an additional hyperdiffusion term. To emulate the conditions of the runs in [7] with the GENE code, for a test we added a fourth-order radial hyperdiffusion term, which is available, but not normally used in the GENE code. The term added to the right hand side of the Vlasov equation is given by

$$D_x = -\epsilon_x (\frac{1}{2}\,\Delta x\, k_x)^4 f, \tag{9}$$

where f is the distribution function. The expression in the parentheses is chosen such that the prefactor ϵ_x does not have to be adjusted when changing resolution. Nonlinear simulations with finite ϵ_x do indeed show smooth ballooning in the transport profile as well as in the temperature, density and potential fluctuation amplitudes, similar to the simulation from Ref. [7]. In Fig. 6, a nonlinear scan over ϵ_x is shown, which demonstrates a clear dependence of the magnitude of ballooning on the hyperdiffusion coefficient ϵ_x.

As these results show, although turbulence codes with a completely spectral perpendicular treatment can not employ the shifted metric, correct simulation results can be achieved even for highly sheared flux tubes, provided that a non-diffusive dealiasing scheme, along with the necessary resolution, is employed. A lack of resolution, on the other hand, can be recognized rather easily in the parallel profiles.

E. Studies with real space treatment of the radial direction

In a nonlocal turbulence code, only the y direction can be computed in Fourier space, so that the Orszag scheme can not be applied to the radial direction anymore, and different antialiasing mechanisms have to be employed. We study such a setup with the nonlocal version of GENE , which computes radial derivatives using fourth-order centered differences.

When emulating the Orszag dealiasing scheme in real space through Lagrange interpolation to a finer grid, it achieves, unlike in Fourier space, only a partial elimination of aliasing effects [23], allowing one to use a smaller coefficient for the hyperdiffusive term. A saturated nonlinear simulation without such a term was not achieved, however. This difference in behavior can be attributed to the local nature of the finite-difference scheme, which yields only finite-order accuracy while the spectral derivatives are given through an expansion in global basis functions, achieving arbitrary accuracy. In analogy to the Fourier version, the real space hyperdiffusion term is here given by:

$$D_x = \epsilon_x \left(\frac{d^4 f}{dx^4} \right) \tag{10}$$

To quantify the spurious ballooning found in a real-space simulation with standard metric, a resolution scan was conducted. For simplicity, we chose again a sheared slab geometry with a global shear value of $\hat{s} = 2$ and a radial box length of $L_x = 80\varrho_i$. This specific value of L_x was chosen to allow for the use of periodic radial boundary conditions for comparison with the shifted metric. For each chosen resolution, a scan in ϵ_x was performed to find the lowest possible value of hyperdiffusion with which a saturated simulation could be achieved. Figure 7 shows the results of the resolution scans with and without shifted metric. The curves labeled only by n_x are runs which use the nonlocal version of GENE with standard metric, emulating the local code setup. As can be seen, increasing the radial resolution increases the accuracy with which slab modes are represented, but completely flat heat flux profiles can, for this shear value and box length, not even be achieved

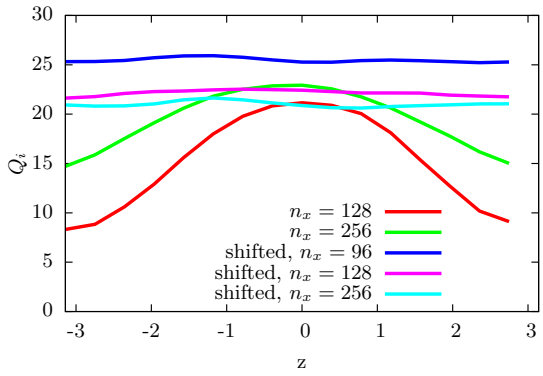

FIG. 7: (Color online) Parallel heat flux profiles with and without shifted metric in the nonlocal code version.

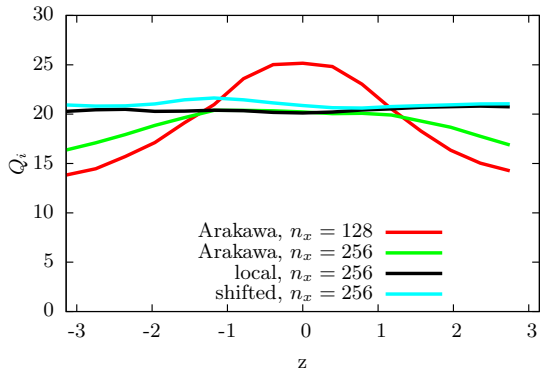

FIG. 8: (Color online) Parallel heat flux profiles with an Arakawa-type nonlinearity, the Fourier-space code version and the nonlocal version with shifted metric.

for 256 radial grid nodes, making converged simulations very expensive. A sixth-order centered difference scheme was also tested in conjunction with a sixth-order hyperdiffusion term, but this yielded only marginally better results than the corresponding fourth-order runs.

With shifted metric, even for relatively low resolution an accurate representation of the slab heat flux profile is obtained, shown here for three different radial resolutions.

F. Influence of the nonlinearity representation

Another test involved the implementation of an Arakawa-type nonlinearity [24], which is used here in a mixed real-space/Fourier-space version which was given in Ref. [25]. The implemented term is

$$\mathcal{N} = \frac{1}{3}\Big[\left(ik_y\chi\frac{\partial g_j}{\partial x} - \frac{\partial \chi}{\partial x}ik_y g_j\right) + ik_y\left(\chi\frac{\partial g_j}{\partial x} - g_j\frac{\partial \chi}{\partial x}\right) + \frac{\partial}{\partial x}\left(g_j ik_y\chi - \chi ik_y g_j\right)\Big], \quad (11)$$

where the quadratic terms in the parentheses are computed in real space in both x and y directions. It was found that nonlocal simulations with the Arakawa-type nonlinearity can achieve stable nonlinear saturation even when running without an additional radial hyperdiffusion term, yielding very robust code operation. However, in such simulations some spurious oscillations occur at the smallest scales, which should be prevented by a small hyperdiffusion contribution to yield more physical results.

The same resolution scan as mentioned above was done with the Arakawa-type nonlinearity in order to find out whether this yields improvement over the standard treatment. The parallel heat flux profiles for different radial resolutions are shown in Fig. 8. As can be seen, the spurious ballooning effect is not completely avoided, but clearly reduced when compared to the standard implementation. In addition, the transport values of the runs with the Arakawa representation are somewhat closer to the converged values. Also shown in the figure is the comparison between the converged local (Fourier) simulation and the shifted metric simulation at the same resolution, which coincide very well.

IV. DISCUSSION

A. Understanding the effect of artificial ballooning

To shed some light on what causes the spurious ballooning induced by radial hyperdiffusion, we will now examine a nonlinear slab run without radial hyperdiffusion (conducted with the local GENE version)—i.e. a run where the transport profiles found in our simulations are flat, as they should be. In the GENE postprocessing tool, one can produce z-profiles not only of transport quantities, but also of the fields and various moments of the distribution function. Adding all contributions, one arrives at flat profiles as expected; however, when fixing k_y to a single value and examining specific k_x modes of the electrostatic potential, these can be found to exhibit peaked parallel profiles with a relatively short parallel correlation length. The peak position depends on the value of k_x one is studying (see examples in Figures 9 and 10).

The peaked behavior of each perpendicular mode (k_x, k_y) is directly linked to the drive that each of these mode pairs is subjected to: In Fourier space, the gyroaveraged potentials, which determine the strength of the gradient drive, are calculated by just multiplying the potential with a Bessel function $J_0(k_\perp^2\varrho^2)$. Here, ϱ is the gyroradius and $k_\perp^2$ is given by

$$k_\perp^2 = g^{xx}k_x^2 + 2g^{xy}k_xk_y + g^{yy}k_y^2. \quad (12)$$

Since $g^{xx} = 1$, $g^{xy} = \hat{s}z$ and $g^{yy} = 1 + \hat{s}^2z^2$ in a straight metric slab, $k_\perp^2$ is a parabola. When varying k_x, the position of the parabola's apex at $z_0 = -k_x/(\hat{s}k_y)$—where the mode experiences the strongest drive—is shifted along the field line. Thus, the ballooning caused by radial hyperdiffusion becomes understandable: While the $k_x = 0$ mode peaks at the center of the flux tube, the higher k_x modes that peak off the center are increasingly damped and the total profile becomes peaked. As shear is increased, modes which peak at a specific position

z_0 have an ever higher k_x and therefore experience stronger damping, explaining the stronger spurious ballooning effect.

Let us now examine Figures 9 and 10 more closely: Fig. 9 was done with the local version of GENE and with a rather large value of hyperdiffusion, while Fig. 10 was done with zero hyperdiffusion, as is standard in the code. Both figures show, for $k_y\varrho_s = 0.75$, the same k_x modes with the values $k_x\varrho_s = 0, \pm 0.942, \pm 1.885$, where the mode with central peak is the $k_x = 0$ mode and the other peaks depart from the center with increasing $|k_x|$. As is clearly visible, in Fig. 9, with activated hyperdiffusion, the modes that peak off the center are rather strongly damped and their peak positions altered, coinciding with a peaked transport profile (solid line in the Figure). On the other hand, in Fig. 10, where hyperdiffusion is turned off, there is no damping of finite-k_x modes and therefore the resulting transport profile is flat.

Considering the impact hyperdiffusion has on modes with finite k_x, one can expect a strong impact also on the heat flux spectra. Indeed, Figs. 11 and 12 show some qualitative differences. While the k_x spectra look very similar for $k_x \lesssim 1$, there is a significant change of behavior for $k_x \gtrsim 1$: Whereas the undamped spectrum decays in a roughly straight line, the fall-off of the damped spectrum is strongly curved, so that the difference quickly becomes several orders of magnitude. This stronger fall-off is what disturbs the slab character of turbulence.

In the k_y spectrum, although not directly affected by radial hyperdiffusion, there are still some differences to be found: While the deviation of the x-damped spectrum from the undamped case is much weaker than in the k_x spectra, the difference between both cases is still an order of magnitude at the high-k end of the spectrum. On the other hand, the coincidence of the curves for lower k_y values is not as good as in the radial spectra. The transport peak is slightly shifted toward lower k_y, while the spectral heat flux density differs by up to a factor of two for the lowest k_y. The overall heat flux, however, is barely affected by these deviations: For the 'clean', unballooned case, we find an ion heat flux of 11.0 ± 1.0 in units of $v_{ti}\varrho_i^2/(n_i T_i L_\perp)$, while in the ballooned case the value is 10.7 ± 1.2.

Applying these results to the situation of the local Fourier code, it is easy to understand the origin of the zig-zag structures observed in Fig. 3: Although there is no explicit k_x-dependent damping in the code, all unresolved modes are set to zero. At too low radial resolution, as is the case in our first simulation, these modes will couple strongly to the modes that are taken into account, affecting the computation of parallel derivatives near the parallel boundaries.

B. Understanding the correction via shifted metric

Having discussed the effect which radial hyperdiffusion has on turbulence simulations in slab geometry, it is now straightforward to see how the shifted metric approach can avoid peaked profiles even with a dissipative numerical scheme. For easier understanding, we provide an explanation in terms of k_x and k_y modes instead of viewing the problem in real space.

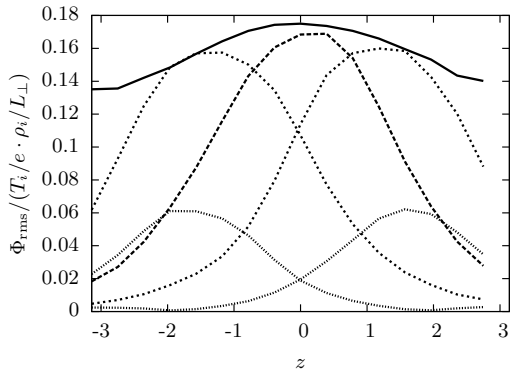

FIG. 9: Time-averaged electrostatic potential for $k_y\varrho_s = 0.75$ and $k_x\varrho_s = 0$ (dashed), $k_x\varrho_s = \pm 0.942$ (shorter dashes) and $k_x\varrho_s = \pm 1.885$ (dotted) for a nonlinear simulation with $\epsilon_x = 10$. The solid line shows the rescaled overall heat transport, which exhibits unphysical ballooning.

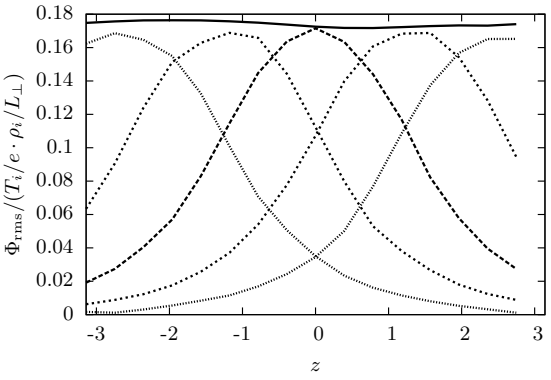

FIG. 10: Time-averaged electrostatic potential for $k_y\varrho_s = 0.75$ and $k_x\varrho_s = 0$ (dashed), $k_x\varrho_s = \pm 0.942$ (shorter dashes) and $k_x\varrho_s = \pm 1.885$ (dotted) for a nonlinear simulation with $\epsilon_x = 0$. The solid line shows the rescaled overall heat transport, which is flat as expected in slab geometry.

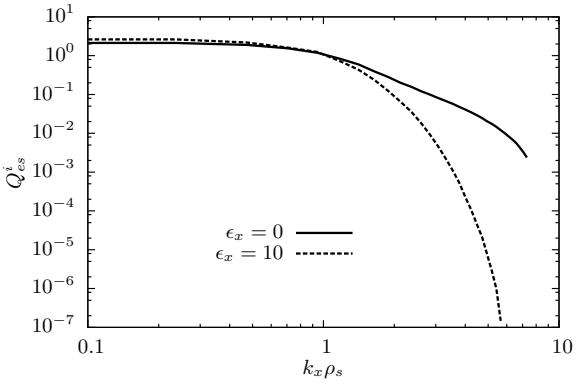

FIG. 11: k_x spectra of the heat flux found in simulations with ($\epsilon = 10$) and without ($\epsilon = 0$) radial hyperdiffusion. As can be seen, for $k_x\varrho_s \gtrsim 1$ there are significant differences, leading to ballooned parallel transport profiles.

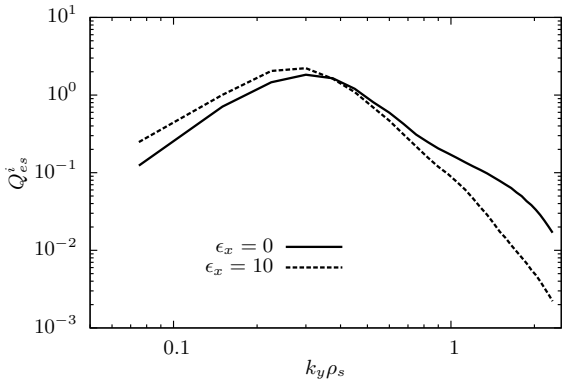

FIG. 12: k_y spectra of the heat flux found in simulations with ($\epsilon = 10$) and without ($\epsilon = 0$) radial hyperdiffusion. The differences here are more subtle, but towards the high-k end of the spectrum the heat flux is significantly damped, while it is somewhat enhanced at low k_y.

With the straight metric approach, magnetic shearing is taken into account via the shape of the flux tube, i.e. the flux tube is twisted when following the field line. Thus, when calculating parallel derivatives, one can use the values from the same k_x mode, since the shearing is automatically included. In the shifted metric approach, however, the flux tube is not deformed, but the shearing must 'manually' be taken into account by applying the k_x shifts discussed above (see Figures 13 and 14 for an illustration). The radial (hyper-)diffusion term, on the other hand, is proportional to some (even-numbered) power of k_x, regardless of whether the straight or shifted metric is used. When using straight metric, the dissipation for a particular k_x mode, is equally strong over the entire parallel length of the flux tube. With shifted metric, the same is true, but the k_x value used to refer to one sheared eddy depends on the parallel position, and thus the damping of that mode also varies.

As shown above, the parallel transport profile in slab geometry consists of many single peaks that are added up. With straight metric and hyperdiffusion, modes with finite k_x are damped, so that the transport profile is affected only off the center position (since this is where the $k_x = 0$ mode peaks). With shifted metric, on the other hand, the metric is changed such that the modes which have a constant finite k_x in straight metric, pass through $k_x = 0$ exactly where they peak. This way, the peak of one mode is always undamped, instead only its tails are damped, resulting in a flat overall transport profile.

Another way to put it is that while with straight metric hyperdiffusion is aligned with the modes (since the grid on which hyperdiffusion is applied is sheared along with the eddies), with shifted metric, the hyperdiffusion is (as is the grid) dealigned from the sheared modes and thus procures equal damping to each mode and does not 'prefer' particular ones. A possibility to avoid introducing dependencies that are not there in the original system is the usage of a dissipation term proportional to $k_\perp^{2n}$ ($n = 1, 2, \dots$), since $k_\perp$ is a physical wavenumber, independent of the coordinates used to describe the system. Furthermore, if only a radial dissipation is desired, one can employ a term proportional to $k_r^{2n} = (k_x + k_y g^{xy}/g^{xx})^{2n}$.

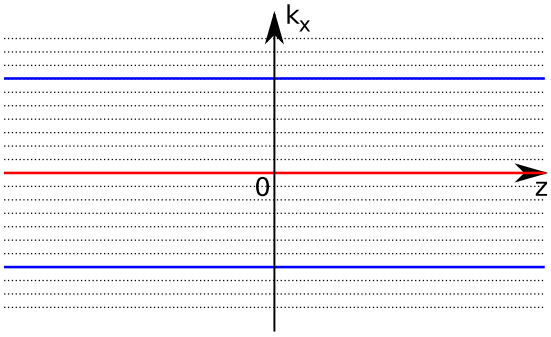

FIG. 13: (Color online) With straight metric, parallel derivatives follow the sheared magnetic field automatically when using the same k_x mode, and a large shift has to be applied at the ends of the z domain in order to connect to beyond the flux tube end.

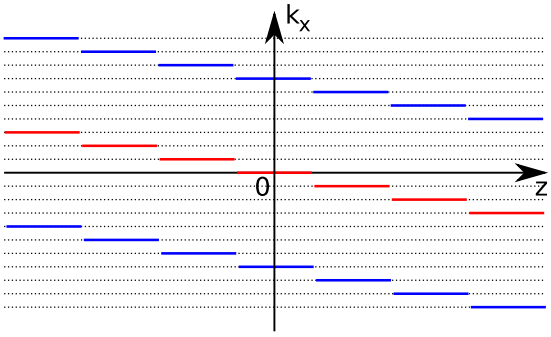

FIG. 14: (Color online) With shifted metric, a small k_x shift has to be applied from each parallel position to the next in order to follow the sheared magnetic field, and periodic boundary conditions suffice to connect to the next flux tube. In straight metric, the mode drawn in the picture would correspond to $k_x = 0$ all along the flux tube.

C. Invariance of physics regarding the shifted-metric transformation

Finally, we would like to note that shifting the y coordinate does not change the physics contained in the simulation. This can be seen when inserting the coordinate transformation $y_k = y - x \cdot g^{xy}/g^{xx}$ and the shifted $k_x' = k_x + k_y \cdot g^{xy}/g^{xx}$ into Eq. (12), which gives $k_\perp^2$, the Fourier space counterpart to the perpendicular Laplacian which enters the Poisson and Ampere equations. Considering that $g^{\varrho\sigma} = \nabla\varrho \cdot \nabla\sigma$ for $\varrho, \sigma \in x, y, z$, the shifts all cancel to yield the original dependence. The same is true for the nonlinearity as given in Eq. 8 and the perpendicular Jacobian $J^{-1} = g^{xx}g^{yy} - (g^{12})^2 = |\nabla x|^2|\nabla y|^2 - (\nabla x \cdot \nabla y)^2$: One merely transfers part of the z dependence from the metric coefficients to a new z dependence of the radial derivative (giving the shifts in k_x).

However, simulations using either of the two approaches differ in the set of modes which make up the perpendicu-

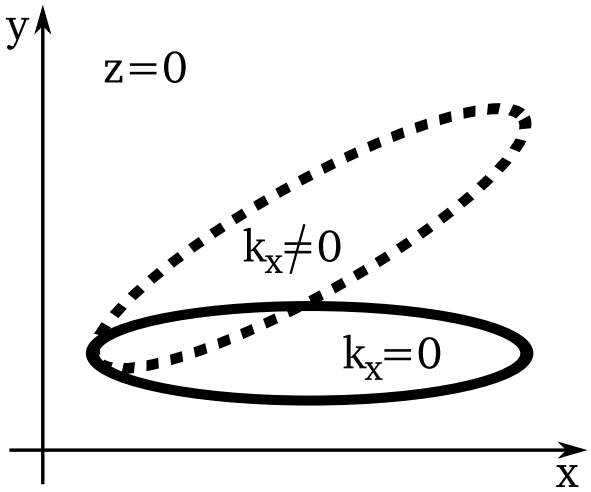

FIG. 15: Perpendicular plane at the reference position $z = 0$, where $\boldsymbol{e}_x \perp \boldsymbol{e}_y$ both for shifted and straight metric.

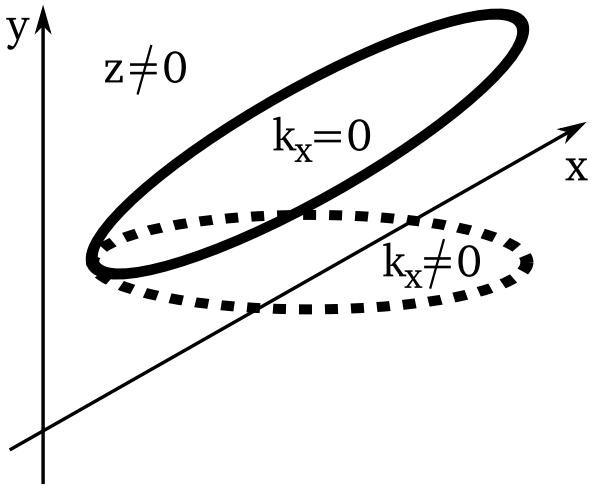

FIG. 16: Straight metric: Perpendicular plane at a finite parallel position $z \neq 0$, where $\boldsymbol{e}_x$ and $\boldsymbol{e}_y$ are no longer orthogonal. Radial hyperdiffusion acts on modes with finite k_x, which are tilted with respect to $\boldsymbol{e}_x$.

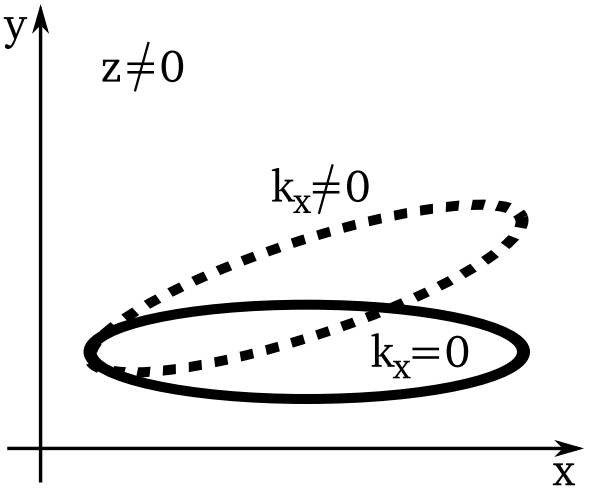

FIG. 17: Shifted metric: Perpendicular plane at a finite parallel position $z \neq 0$. $\boldsymbol{e}_x$ and $\boldsymbol{e}_y$ are still orthogonal, so that radial hyperdiffusion now acts only on modes which do not point radially outward.

lar plane. While with shifted metric, each parallel position has a mode that points radially outward, with straight metric this mode is in general only present at the reference position, where the grid is perpendicular (Fig. 15). At all other positions, the mode labeled $k_x = 0$ is tilted away from the outward direction and the grid has a rhomboid shape (Fig. 16). The direction radially outward is in general only approximately contained in the simulation, and if radial hyperdiffusion were used, this direction would be damped since it is labeled with finite k_x values. In an undamped simulation, on the other hand, modes which follow the sheared field are *not* preferred and a correct treatment of perpendicular dynamics is ensured. Note, however, that such simulations may still require large radial resolutions to take into account all modes which generate relevant transport.

With shifted metric, the situation is inverted: At the reference position, there is no difference to the standard metric, but when going to $z \neq 0$ the grid remains perpendicular. Therefore, in a simulation with dissipation (which is a likely setup for a shifted-metric simulation), the modes which point radially outward are now preferred over the damped $k_x \neq 0$ modes (Fig. 17). Therefore the parallel correlation length of structures which follow the sheared field will suffer some artificial reduction. This is particularly important for small-scale eddies, since the k_x shifts (given by Eq. (7)) are proportional to the k_y wavenumber. A small eddy in a heavily sheared magnetic field thus quickly connects to k_x modes which are not resolved anymore, and is damped to avoid aliasing. Therefore, in situations with large local shear, it must be ensured via convergence tests that the radial resolution is sufficient to represent the evolution of turbulent structures along the field lines correctly.

V. CONCLUSIONS

In this work, we examined the properties of two different approaches to field-aligned coordinate systems. The first approach, which is the well-known field-aligning transformation, generates a coordinate system whose perpendicular coordinates are nonorthogonal in the case of sheared magnetic fields. The other approach is the shifted metric ansatz, which yields a whole set of coordinate systems, one for each position along the field line, each of which is orthogonal in the perpendicular plane.

As was known from earlier work, turbulence simulations employing standard field-aligned coordinates can show spurious parallel dependencies when studying highly sheared magnetic geometries. This effect is found to arise from a lack of radial resolution, and can be amplified by the use of a radial hyperdiffusion term (or a dissipative numerical scheme), which is often used to prevent aliasing effects caused by energy transfer to smaller scales than described by the grid. We studied how the creation of artificial parallel structures can be

prevented in different numerical treatments. Since flux-tube codes which compute the perpendicular dynamics in Fourier space need to use periodic radial boundary conditions, they can not implement the shifted metric approach. However, such codes may be run without hyperdiffusion, if an appropriate dealiasing scheme, e.g. the three-halves rule, is used. Simulations performed in this way do not exhibit the spurious ballooning observed in damped simulations, provided that the radial resolution is high enough. A lack of resolution, on the other hand, leads to zig-zag structures in the parallel profiles and is thus easily identifiable, a property that can be important when there is also physical ballooning, e.g. in toroidal geometry.

In nonlocal codes, on the other hand, the radial boundary conditions can not be periodic, excluding the use of Fourier schemes. Therefore, to avoid aliasing effects, one has to resort to a numerical diffusion term, which can, as shown above, lead to the creation of artificial parallel structure. Although this situation can again be improved by increasing the radial resolution, while at the same time keeping hyperdiffusion as low as possible (possibly using a nonlinearity scheme with low dissipation like the Arakawa discretization), reaching a converged simulation proves more expensive than with a Fourier code.

These codes, on the other hand, offer the possibility to implement the shifted metric approach, which avoids the creation of spurious parallel structures. Still, large local or global shear will lead to strong twisting of the simulated eddies with respect to the box, resulting again in the need to perform convergence checks to ensure sufficient radial resolution.

VI. ACKNOWLEDGEMENTS

The authors would like to thank G.W. Hammett, T. Görler, F. Merz, and M.J. Pueschel for fruitful discussions. The computations have been performed on the BOB cluster and the Power6 computer at the Garching Computing Center.

[1] F. Wagner, G. Becker, K. Behringer, D. Campbell, A. Eberhagen, W. Engelhardt, G. Fussmann, O. Gehre, J. Gernhardt, G. v. Gierke, G. Haas, M. Huang, F. Karger, M. Keilhacker, O. Klüber, M. Kornherr, K. Lackner, G. Lisitano, G.G. Lister, H.M. Mayer, D. Meisel, E.R. Müller, H. Murmann, H. Niedermeyer, W. Poschenrieder, H. Rapp, H. Röhr, F. Schneider, G. Siller, E. Speth, A. Stäbler, K.H. Steuer, G. Venus, O. Vollmer, Z. Yü Phys. Rev. Lett. **49**, 1408 (1982)
[2] J.W. Connor, R.J. Hastie, and J.B. Taylor, Phys. Rev. Lett. **40**, 396 (1978)
[3] P. Xanthopoulos and F. Jenko, Phys. Plasmas **13**, 092301 (2006)
[4] S.C. Cowley, R.M. Kulsrud, R. Sudan, Phys. Fluids B **3**, 2767 (1991)
[5] W.D. D'Haeseleer, W.N.G. Hitchon, J.D. Callen, J.L. Shohet, Flux Coordinates and Magnetic Field Structure (Springer Verlag, Berlin, 1991), p. 100ff.
[6] M.A. Beer, S.C. Cowley, G.W. Hammett Phys. Plasmas **2**, 2687 (1995)
[7] B. Scott, Phys. Plasmas **8**, 447 (2001)
[8] A. Kendl and B.D. Scott Phys. Rev. Lett. **90**, 035006 (2003)
[9] M. Kotschenreuther, G. Rewoldt, and W.M. Tang, Comp. Phys. Comm. **88**, 128 (1995)
[10] W. Dorland, F. Jenko, M. Kotschenreuther, and B.N. Rogers, Phys. Rev. Lett. **85**,5579 (2000)
[11] A.G. Peeters, Y. Camenen, F.J. Casson, W.A. Hornsby, A.P. Snodin, D. Strintzi, G. Szepesi, Comput. Phys. Commun. **180**, 2650 (2009)
[12] F. Jenko, W. Dorland, M. Kotschenreuther, and B.N. Rogers, Phys. Plasmas **7**, 1904 (2000)
[13] T. Dannert and F. Jenko, Phys. Plasmas **12**, 072309 (2005)
[14] F. Merz, Ph.D. thesis, University of Münster, 2008
[15] T. Görler, Ph.D. thesis, University of Ulm, 2009
[16] F. Merz and F. Jenko, Phys. Rev. Lett. **100**, 035005 (2008)
[17] T. Görler and F. Jenko, Phys. Rev. Lett. **100**, 185002 (2008)
[18] M. Kammerer, F. Merz, and F. Jenko, Phys. Plasmas **15**, 052102 (2008)
[19] M.J. Pueschel, M. Kammerer, and F. Jenko, Phys. Plasmas **15**, 102310 (2008)
[20] A.M. Dimits, G. Bateman, M.A. Beer, B.I. Cohen, W. Dorland, G.W. Hammett, C. Kim, J.E. Kinsey, M. Kotschenreuther, A.H. Kritz, L.L. Lao, J. Mandrekas, W.M. Nevins, S.E. Parker, A.J. Redd, D.E. Shumaker, R. Sydora, and J. Weiland, Phys. Plasmas **7**, 969 (2000)
[21] P. Colella, D.T. Graves, B.J. Keen, and D. Modiano, J. Comput. Phys. **87**, 171 (1990)
[22] S. Orszag, J. Atmos. Sci. **28**, 1074 (1971)
[23] X. Lapillonne, T. Dannert, S. Brunner, A. Marinoni, S. Jolliet, L. Villard, F. Jenko, T. Goerler, F. Merz, AIP Conf. Proc. **1069**, 289 (2008)
[24] A. Arakawa, J. Comput. Phys. **1**, 119 (1966)
[25] J. Candy, R.E. Waltz J. Comput. Phys. **186**, 545 (2003)